Superconductor Science and Technology

ACCEPTED MANUSCRIPT • OPEN ACCESS

Precise determination of oxygen content in SmBa2Cu3O7-δ thin film samples using x-ray diffraction

To cite this article: Kai Walter *et al* 2024 *Supercond. Sci. Technol.*

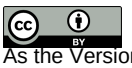

Precise Determination of Oxygen Content in $SmBa_2Cu_3O_{7-\delta}$ Thin Film Samples using X-ray Diffraction

Authors: Kai Walter[1], kai.walter@kit.edu; Manuela Erbe[1], manuela.erbe@kit.edu; Alexander Welle[2,3], alexander.welle@kit.edu; Jens Hänisch[1], jens.haenisch@kit.edu; Bernhard Holzapfel[1], bernhard.holzafpel@kit.edu

[1] Institute For Technical Physics, Karlsruhe Institute of Technology, Hermann-von-Helmholtz-Platz 1, Eggenstein-Leopoldshafen, 76344 Germany
[2] Institute of Functional Interfaces, Karlsruhe Institute of Technology, Hermann-von-Helmholtz-Platz 1, Eggenstein-Leopoldshafen, 76344 Germany
[3] Karlsruhe Nano-Micro Facility, Karlsruhe Institute of Technology, Hermann-von-Helmholtz-Platz 1, Eggenstein-Leopoldshafen, 76344 Germany

1. Abstract

The superconducting properties of $SmBa_2Cu_3O_{7-\delta}$ (SmBCO) thin films are predominantly influenced by the oxygen deficiency δ. Yet, the established methods to determine δ such as iodometric titration or thermogravimetry cannot be applied to thin films due to their very small volume.
Therefore, an alternative way to determine δ for SmBCO thin film samples using X-ray diffraction (XRD) is presented. Main point of this analysis is the structural relationship between the *a*, *b* and *c* lattice parameters and δ. A linear relationship between *c* and δ is found in SmBCO powder samples for both the orthorhombic and tetragonal phases.
Furthermore, an attempt is made to quantify the chemical composition using Time-of-Flight Secondary Ion Mass Spectrometry (ToF-SIMS). This attempt was inconclusive because of drastically changing ion yields due to δ influencing the valence state of the analyzed ions.
The found crystal structural relationship gathered from the powder samples is applied to thin film samples. Thereby, it becomes clear that thermal strain is affecting the crystal structure of the thin films. A simple correction model is used to correct for thermal strain and a good match between powder, literature and thin film data is achieved and thus a non-destructive way for the determination of δ using XRD.

Keywords: SmBCO, CSD, Oxygen Deficiency, XRD

2. Introduction

Rare Earth Barium Copper Oxides (REBCO) are among the most researched superconductors since their discovery in the late 1980s. Their remarkably high critical Temperatures (T_c) and high critical current densities (J_c) make them ideal candidates for several power and magnet applications in the form of Coated Conductors (CC) [1–3].
A recent comparative study on Chemical Solution Deposition (CSD) [4] showed that high T_c and J_c values can be achieved for different REBCO (RE = Sm, Gd, Dy, Y, Er) thin film samples using the same preparation method. The performance of $SmBa_2Cu_3O_{7-\delta}$ (SmBCO) was therein surprising. Over a large processing window, high T_c values of over 94 K and relatively high J_c

values were achieved. Erbe et al. acknowledged in their study that the oxygenation process and the oxygen load of the samples were not systematically investigated as determining the oxygen deficiency δ on thin film samples is not as trivial as to be expected. As a continuation, this paper aims to tackle the problem of precisely determining δ of REBCO thin films exemplarily on SmBCO films.

Very early research on REBCO systems indicated that the oxygen content or in other words the oxygen deficiency δ play a major role in defining the superconducting properties, as the crystal structure transitions from orthorhombic (*Pmmm*, 47) at low δ to tetragonal (*P4/mmm*, 123) at high δ. This O/T transition was systematically investigated for many REBCO systems (RE= La, Nd, Sm, Eu, Gd, Dy, Ho, Y, Er, Tm, Yb) by Kubo and Nakabayashi et al. [5, 6]. They concluded that the O/T transition, characterized by a transition temperature $T_{O/T}$ and a critical oxygen deficiency (δ_c), depends mainly on the repulsion energy V of the nearest-neighbor oxygen sites in the *ab*-plane and on the partial pressure of oxygen pO_2. They derived the following equation:

$$k_B T_{O/T} = (1-\delta_c^2) \cdot V \qquad 1$$

For SmBCO, this postulates a gradually decreasing transition temperature $T_{O/T}$ for increasing δ. Although it is a good approximation, **Figure 1a)** (red curve), this equation does not fully describe the reality of SmBCO, as Kogachi et al. [7, 8] showed shortly after with in-situ X-ray Diffraction (XRD) cooling experiments and T_c measurements of REBCO powder samples (RE= Y, Sm, Gd, Tm): The O/T transition point does not change as significantly as expected according to equation 1 at temperatures below 350 °C, likely due to kinetic effects, and clearly, the O/T transition behavior depends on the ionic radius of the RE ion. The height of the so-called T_c plateau at medium δ values, and δ_c, extrapolated towards room temperature, clearly decrease with increasing ionic radius, **Figure 1b,c)**. Their investigations claim that SmBCO exhibits a δ_c at room temperature of 0.6 and should show a T_c plateau of 45 K at medium δ values.

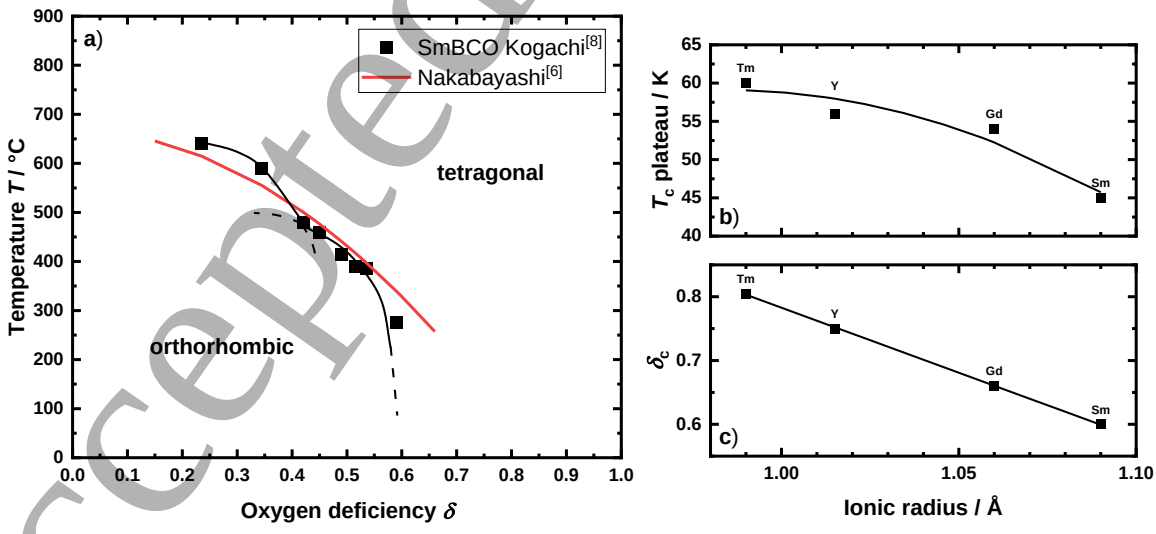

Figure 1: Characterization of the O/T transition by Kogachi et al and Nakabayashi et al. **a)** Temperature vs δ, comparison of Refs. [8] and [6] (equation 1). **b,c)** Height of the T_c plateau and δ_c at temperatures below 300 °C depend on the RE ionic radius, taken from Ref. [7].

Furthermore, Kogachi et al. showed how the lattice parameters *a*, *b*, and *c* relate to *δ*. The *c* lattice parameter, often called *c*-axis, increases linearly both in the orthorhombic and tetragonal phase region. The O/T transition can be identified by a sudden *c*-axis increase and the equalization of the lattice parameters *a* and *b*. This behavior agrees very well with data of other REBCO systems, such as YBCO [9–11].
The reason for this crystallographic change is the redistribution of oxygen from ordered Cu-O chains along the *b*-axis to equivalent but previously vacant sites along the *a*-axis, resulting in a disordered state of Cu-O plains perpendicular to the *c*-axis. Consequently, the O/T transition can be understood as an order/disorder transition. Evaluating the powder data of Refs. [7–12] reveals that the sharpness of the O/T transition strongly depends on the sample preparation. While powder samples heat-treated at high temperatures usually show a continuously increasing *c*-axis, powder samples heat-treated below 400 °C show a discontinuous *c*-axis increase at the O/T transition. Cava et al. [10, 12], who observed a discontinuous *c*-axis change, argue that high temperature diffusion heat treatments and subsequent cooling introduce non-equilibrium oxygen disorder in the *ab*-plane. Such non-equilibrium samples should show lower T_c and broader transition ranges as well as a smoothed-out *c*-axis discontinuity. Investigations of the effect of Cu-O disorder on the charge carrier density and consequently T_c by Claus et al. [13] and Veal et al. [14] confirmed this. They showed that increasing disorder distorts the shape and height of the T_c plateau, which complements the crystallographic data.

In this paper we show how the relationship between the lattice parameters *a*, *b*, and *c* and the oxygen deficiency *δ* can be established with powder and thin film samples by using XRD and low temperature heat treatments and attempted Time-of-Flight Secondary Ion Mass Spectrometry (ToF-SIMS). Through the obtained relationship, the oxygenation state of a particular REBCO compound, here SmBCO, can be evaluated simply by using XRD and T_c measurements. This simple method of determining *δ* lends itself to be used in on-line application for the production of CC and enables more comprehensive analyses of thin film samples to further understand the connection of microstructure and superconductivity.

3. Methods

Powder samples were used to establish the crystal structural relationship between the lattice parameters *a*, *b* and *c* and the oxygen deficiency δ, which was later used to determine δ of thin film samples.

The oxygen deficiency of each powder sample was calculated using the mass loss during heat treatment (HT) in a flowing Ar atmosphere. The total mass loss during HT can be split into two parts: adsorbed moisture and loss of oxygen, while assuming that no chemical reaction takes place. This was confirmed by analyzing the powder XRD patterns for phases other than SmBCO. Thereby, the change in oxygen deficiency, $\Delta\delta$, can be directly calculated as:

$$\Delta\delta = \frac{\Delta m_O}{M_O * n(\mathrm{SmBCO})}$$

from the oxygen loss during HT Δm_O, the molar mass of oxygen M_O and the amount of substance of the weighted-in SmBCO n(SmBCO). Varying HT temperatures were used to achieve varying δ while keeping the HT time and partial pressure of oxygen pO_2 constant at 120 min and 0 bar, respectively. For each of these powder experiments, 500 mg SmBCO powder by Toshima Manufacturing with 99.9% purity and an average grain size of 10 µm was used. All thermogravimetry experiments were performed using a NETZSCH STA 449C Jupiter equipped with a thermogravimetry analysis (TGA) Al_2O_3 crucible.

The total oxygen deficiency δ can only be determined if the starting oxygen deficiency δ_0 of the powder is known because the method stated above can only determine changes in δ but not the total δ. The starting oxygen deficiency δ_0 of the delivered powder was determined from the mass loss by reduction in Ar+5% H_2 at 800 °C following the reaction:

$$2\ \mathrm{SmBa_2Cu_3O_y} + (2y\text{-}7)\ \mathrm{H_2} \rightarrow \mathrm{Sm_2O_3} + 4\ \mathrm{BaO} + 6\ \mathrm{Cu} + (2y\text{-}7)\ \mathrm{H_2O}$$

This experiment was done twice to check for reproducibility. The same δ_0 was calculated for both tries. Slight adjustments to the stoichiometry of the produced oxides were necessary, as traces of $BaSm_2O_4$ and $BaSm_2CuO_5$ were found in the produce. The starting value δ_0 of the delivered powder was thus calculated to be 0.05. This was confirmed by oxygen loading experiments on the same powder, in which the pristine powder absorbed oxygen equating to a $\Delta\delta$ of -0.048, illustrating precision and certainty of δ_0. Nonetheless, the total accuracy of δ needs to be given with 0.02 as differences in samples handling, adsorbed moisture and crucible calibrations result in slight changes of the observed weight changes.

To study the structural relationship between the lattice parameters *a*, *b* and *c* and the oxygen deficiency δ, pristine powder samples were heat-treated for 120 min in an Ar atmosphere at a pressure of 1 bar (pO_2 = 0 bar) and various heat treatment (HT) temperatures of 300-800 °C, with respective heating and cooling rates of 20 °Cmin^{-1}. The mass loss during the HT was recorded, corrected for absorbed moisture, and the corresponding oxygen deficiency after the HT was calculated.

For the Chemical Solution Deposition (CSD) of SmBCO thin film samples, trifluoroacetate metal organic deposition (TFA-MOD) solutions were used. Those are based on methanol as a solvent and a 1:2:3 ratio of Sm, Ba and Cu and a total molar amount of 1.5 mol l^{-1} overall cations. The chemistry of the solutions is described in detail in Ref. [15].

These solutions were spin-coated on cleaned 10 × 10 mm^2 [100]-oriented $LaAlO_3$ (LAO) single crystal substrates with a rotation speed of 6000 rpm for 30 s to achieve a film thickness of

200(15) nm. After coating, the samples were pyrolyzed and crystallized. The crystallization was performed at 820 °C with a constant p_{O2} of 50 ppm. Subsequently, the samples were oxygenated at 450 °C. This procedure is described in detail in Ref. [15].

For the oxygen out-diffusion experiments, the thin film samples were placed under flowing N_2 at 1000 ml min^{-1} and heated to 300 or 350 °C, depending on the sample set. The samples thereby experience a mean heating/cooling ramp of 21/33 °C min^{-1} respectively. The timer for each HT step was started when 90 % of the target temperature (in °C) was reached. The HT time for each thin film sample was thus gathered accumulatively.

All samples were characterized after each HT step of usually 5-60 min. The lattice parameters of the powder samples were determined with XRD using a 3 kW Bruker D8 Discover system. Cu Kα radiation, filtered for K_β, at 40 kV and 40 mA was used in Bragg-Brentano geometry to gather θ/2θ scans. A LYNXEYE_XE detector was used in 1D mode to improve the quality of the signal. Smartlab Studio II by Rigaku was used for the Rietveld refinement.

The lattice parameters of the thin films were determined with XRD using a Rigaku Smartlab 3 kW. Monochromatic Cu $K\alpha_1$ radiation at 40 kV and 30 mA was used in parallel-beam geometry to minimize sample misalignment. A HyPix3000 detector was used in 0D mode to collect as much intensity as possible, as the investigated skewed peaks exhibited relatively low intensity compared to the θ/2θ scans of the thin films. θ/2θ scans were employed to determine the *c*-axis lattice parameter with the Nelson-Riley method [16] using all available [00L] peaks between 5 and 120°. The (30$\underline{1}$0)/(03$\underline{1}$0) and (136)/316) peak pairs were measured with ω/2θ scans in asymmetric ϕ-geometry [17] and used to determine the lattice parameters *a* and *b* following the procedure by Wimbush et al. [18].

The superconducting state of the powder samples was evaluated by Vibrating Sample Magnetometry (VSM) in a DynaCool Physical Property Measurement System (PPMS) by Quantum Design. Therein, the magnetic moments of the zero-field-cooled (ZFC) samples, weighing 50 µm each, were measured over temperature *T*. T_c^{onset} was defined as the point at which the initial magnetic moment was fully compensated to become zero.

The superconducting state of the thin films was evaluated by inductive T_c measurements. They were carried out with a 14-T Quantum Design PPMS and a self-designed and calibrated mutual inductance device. The transition is characterized by the values T_c^{90} and T_c^{10}, which are defined as the temperatures at which the voltage is 90 % and 10 % of the normal state. The sharpness of the transition is defined as $\Delta T_c = T_c^{90} - T_c^{10}$.

The chemical composition of representative samples was analyzed using Time-of-Flight Secondary Ion Mass Spectrometry (*ToF-SIMS*). *ToF-SIMS* was performed on a TOF.SIMS5 instrument (ION-TOF GmbH, Münster, Germany) equipped with a Bi cluster primary ion source and a reflectron-type time-of-flight analyzer. UHV base pressure was < 3.4×10^{-9} mbar. For high mass resolution and sensitivity, the Bi source was operated in "high current bunched" mode providing short Bi^+ primary ion pulses at 25 keV energy, a lateral resolution of approx. 4 µm, and a target current of 1.4 pA at 10 kHz repetition rate. The short pulse length of 1.5 ns allowed for high mass resolution. The primary ion beam was rastered across a 300×300 μm^2 field of view on the sample, and 128×128 data points were recorded. For depth profiling a dual beam analysis was performed in interlaced mode (each pause in between individual shots of the primary ion source were used for erosion): Therefore, a 2 keV cesium erosion beam was scanned over a concentric field of 500×500 μm^2 on the sample. Having a sputter beam current (pulsed) of 88 to 90 nA (readjusted after each analysis), this ion bombardment effectively erodes the sample. The analysis was stopped after the substrate was reached as evidenced by a drop of SmBCO signals and rising signals of AlO, AlO_2, LaO, and LaO_2.

4. Results

In **Figure 2**, the determined lattice parameters, **Table 1**, and T_c^{onset} of the powder samples are plotted over the oxygen deficiency δ calculated via mass loss. The samples heat-treated below 450 °C remain orthorhombic and superconducting. Their *c* lattice parameters increase from 11.7278(4) to 11.7575(4) Å for δ = 0 to 0.29, respectively, while the lattice parameters *a* and *b* stay constant at 3.8599(33) Å and 3.9050(23) Å, respectively. T_c drops from 94.8(2) K to 48.6(5) K over the orthorhombic range.

All powder samples heat-treated at and above 500 °C were tetragonal and thus non-superconducting. These samples show a significantly increased *c* lattice parameter between 11.8119(3) and 11.8532(2) Å for δ = 0.52 to 0.95. The lattice parameters *a* and *b* stay equal and constant at 3.8879(31) Å in that range.

We find clear linear trends (dashed lines in **Figure 2a)**) of the *c* lattice parameter in the orthorhombic and tetragonal regions, respectively. The 450 °C sample at δ = 0.42 seems to be in a transitional state between the two regions as the Rietveld refinement did not identify a highly orthorhombic or tetragonal structure. Additionally, the 450 °C sample does not exhibit a T_c^{onset} down to 5 K.

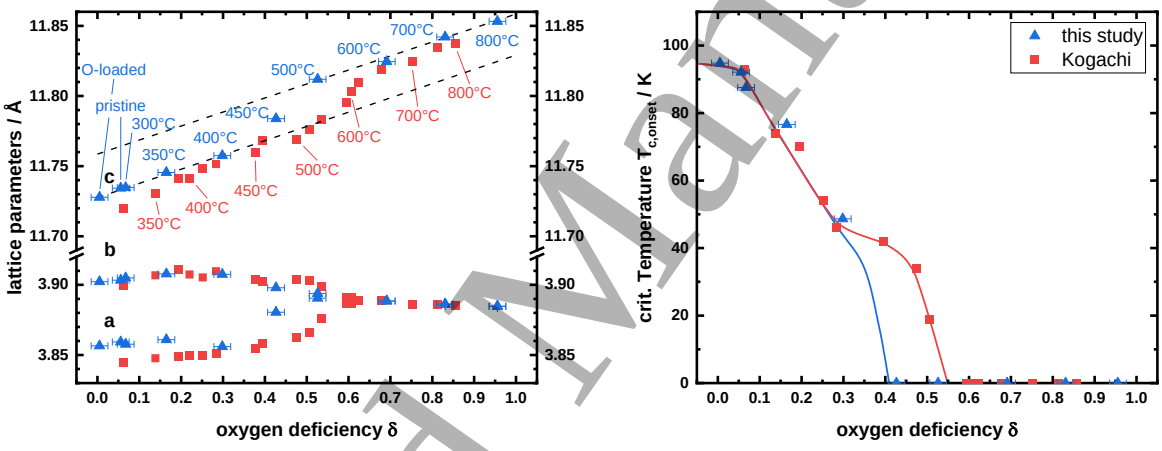

Figure 2: Results of the powder sample analysis of this study (blue triangles), compared to Kogachi et al. [7] (red squares). **a)** Dependence of SmBCO powder crystal structure on oxygen deficiency adjusted via HTs at different *T*. Linear trends (dashed lines) are fitted to the orthorhombic and tetragonal phases. **b)** T_c^{onset} of the same powder samples.

Table 1: Rietveld refinement results of the SmBCO powder samples for the orthorhombic *Pmmm* and tetragonal *P4/mmm* space group. The statistical standard deviation of the last digit is given in parentheses. The fitted curves are available in the supplementary information.

δ	0.008	0.056	0.068	0.165	0.298
a / Å	3.8565(3)	3.8593(2)	3.8577(8)	3.8609(6)	3.8560(5)
b / Å	3.9023(2)	3.9033(1)	3.9050(4)	3.9078(2)	3.9075(5)
c / Å	11.7278(4)	11.7343(3)	11.7347(2)	11.7455(2)	11.7575(4)
V / Å^3	176.49	176.77	176.77	177.21	177.16
cryst. size / Å	665(6)	614(4)	902(6)	603(4)	907(9)
R_{wp} / %	9.47	15.23	9.42	10.60	9.13
R_p / %	6.35	9.40	6.57	6.55	5.81
δ	0.426	0.526	0.691	0.830	0.955
a / Å	3.8805(3)	3.8905(4)	3.8884(1)	3.8862(5)	3.8847(2)
b / Å	3.8979(3)	=a	=a	=a	=a

c / Å	11.7838(4)	11.8119(3)	11.8245(4)	11.8420(4)	11.8532(2)
V / Å^3	178.24	178.94	178.79	178.85	178.88
cryst. size / Å	653(5)	1231(9)	1170(6)	1515(12)	1343(8)
R_{wp} / %	13.77	11.23	8.62	9.96	8.71
R_p / %	7.90	6.98	5.58	6.17	5.50

Comparing our powder data to those of Kogachi et al. [7], we see that our samples are more oxygen deficient at the same HT temperature. This is likely a result of Kogachi et al. using a static HT atmosphere and the oxygen partial pressure slowly increasing with HT temperature and time. By that, δ of their powder samples no longer follows the 0 bar isobaric T-δ line. This effect is most prominent at T > 500 °C as the oxygen partial pressure is increasing more and more. In our experiment, any out-diffusing oxygen was carried away by a steady Ar flow. Thus, our powder samples follow the 0 bar isobaric T-δ line more precisely, and higher δ values are reached at the same HT temperature.

Nonetheless, irrespective of the experimental setup, we see that both data sets agree very well for δ = 0 to 0.3 and 0.7 to 1 as those powder samples show the same lattice parameters at the same δ values and follow the linear trends established from the data presented in this study. A striking difference between both data sets occurs for δ = 0.4 to 0.6. Our samples heat-treated at 450 and 500 °C at δ = 0.42 and 0.52 are transitioning or already tetragonal. The powder samples of Kogachi et al. are orthorhombic at these HT temperatures and δ. Their O/T transition can be seen at δ = 0.6. Comparing these HT temperatures and δ values with the data presented in **Figure 1a)**, one realizes that our samples are exactly behaving as **Figure 1a)** would suggest, because δ of any sample heat-treated above 450 °C is larger than δ_c at the respective temperature and was found to be tetragonal. The powder samples of Kogachi et al. stand in contrast to that. All of their samples heat-treated above 500 °C should be tetragonal according to **Figure 1a)**, yet they are not. We assume that the cooling procedure, which was unfortunately not described in detail in Ref. [7, 8, 19], is responsible for the observed differences. While a rapid quench conserves the high temperature oxygen disorder, a slow cooling process allows for the oxygen order to be reestablished and for orthorhombicity and thus superconductivity to reemerge. This goes to show, that samples of same oxygen deficiency might have completely different oxygen orderings, e.g. due to slow cooling and thus different properties. This can also be seen in the T_c data, **Figure 2b)**. Both data sets agree very well up to δ = 0.3. Our samples do not show any T_c beyond this point. Kogachi's samples show a small plateau at 45 K with T_c disappearing at δ ~ 0.6. Their slow cooling process resulted in the reestablishment of oxygen order at δ ~ 0.4 and thus a reemergence of T_c.

Turning to the pristine thin film samples, we find that our sample preparation procedure is very reproducible because all investigated properties show a small deviation from the mean. θ/2θ scans show that a strong SmBCO (001)/[100]||(001)/[100] LAO texture was achieved, **Figure 3a)**. Furthermore, no shoulder peaks are observed, confirming that only a single SmBCO phase of homogeneous oxygen content is created. ToF-SIMS data also confirms that the oxygen is homogenously distributed throughout the whole 200(10) nm film thickness.

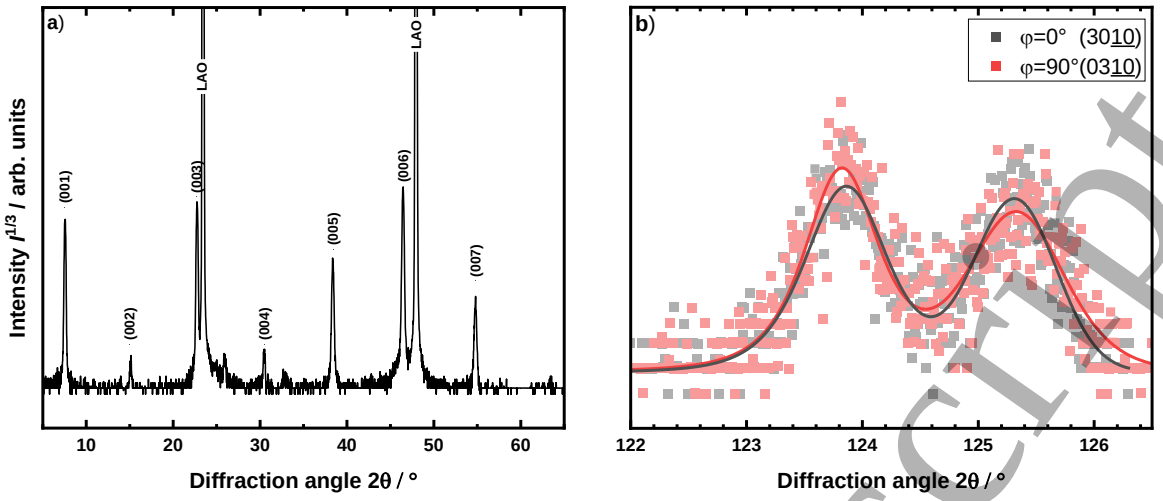

Figure 3: XRD characterization of thin film samples in the pristine state. **a)** θ/2θ scan of a representative sample. Only SmBCO (00*l*) and LAO (*h*00) peaks are detected, indicating a strong heteroepitaxial growth of SmBCO on LAO. The 2θ range has been restricted to 5-70° for better visibility. **b)** ω/2θ scan of the (30$\underline{1}$0)/(03$\underline{1}$0) asymmetric peak pair. A double peak instead of one peak for each ϕ orientation developed due to twins in the *ab*-plane.

The average *c*-axis of the pristine samples, determined via Nelson-Riley [16], is 11.7156(10) Å, which are the smallest values for all sample sets and HT times. To determine the lattice parameters *a* and *b*, the (30$\underline{1}$0)/(03$\underline{1}$0) and (136)/(316) asymmetric peak pairs are measured, fitted and determined using a least mean square approach. As can be seen in **Figure 3b)**, instead of one peak for each phi-orientation, double-peaks for (30$\underline{1}$0) and the 90° phi-rotated (03$\underline{1}$0) was observed. The same is the case for (136)/(316), not shown here. This feature is due to twinning in the *ab*-plane. The pristine samples are clearly orthorhombic with *a* and *b* lattice parameters of 3.8583(10) Å and 3.9082(10) Å respectively. Later on, it will be shown that this domain structure disappears as *a* and *b* become equal during the O/T transition.
T_c^{90} values of 94.5(2) K and ΔT_c of 0.52(25) K are achieved in the pristine state. This is consistent with our XRD and literature data, meaning that the highest T_c corresponds to the smallest *c*-axis. Additionally, small ΔT_c values indicate a uniform oxygen ordering along the Cu-O chains, i.e. the OI phase [20, 21].

With cumulatively increasing HT time at 300 °C, the SmBCO (006) peak clearly shifts towards smaller 2θ values, **Figure 4a)**, which corresponds to an increasing *c*-axis lattice parameter. The LAO substrate peak at around 48° is unaffected by the HT. A decrease in intensity accompanies the SmBCO peak shift. This is in accordance with our structure factor calculations, which predicted a reduction of the maximum intensity for increasing oxygen deficiencies. Furthermore, no secondary SmBCO phase is detected, which indicates that the oxygen content of the samples has been homogeneous after each HT step, which is also confirmed by ToF-SIMS data.

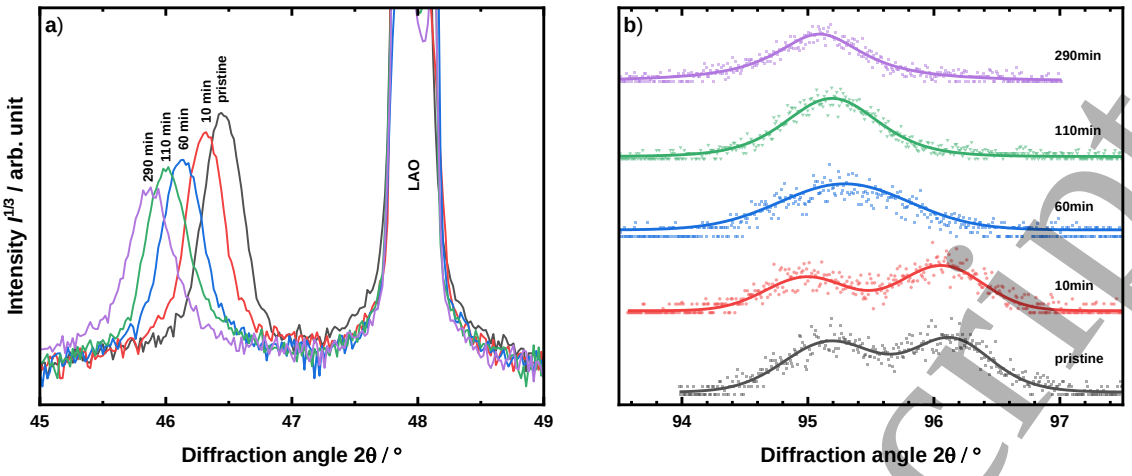

Figure 4: Influence of the cumulative HT time at 300 °C on the crystal structure. **a)** Evolution of SmBCO (006) peak. The peak shift indicates an increasing *c* lattice parameter due to oxygen out-diffusion. **b)** Twin domain evolution shown at the (136) double peak. The samples stay orthorhombic until 60 min. Afterwards, the O/T transition sets in and the two peaks merge into one as the lattice parameters *a* and *b* are getting equal. This process is complete after 110 min. From that point on, only little change can be determined in *a* or *b*.

Also the skewed (30$\underline{1}$0)/(03$\underline{1}$0) and (136)/(316) peak pairs are shifting during HT as shown for (136) in **Figure 4b)**. Both pairs were used for determining *a* and *b*. In the early HT cycles, *a* and *b* stay constant and the visible peak shift in **Figure 4b)** at 10 min is a result of an increasing *c* lattice parameter. Before 60 min and while the *c* lattice parameter is changing drastically, *a* and *b* change only in the margin of error. Around 60 min, the double peak originating from the twin domain structure disappears, a sign that the samples are becoming tetragonal. It should be noted that determining *a* and *b* in the transitioning state, $60 \leq t < 120$ min, is more difficult than in the orthorhombic or tetragonal region, because fitting the combined peak of both domains is prone to error. Therefore, the standard deviation in *a* and *b* for transitioning samples is higher than for orthorhombic or tetragonal samples, **Figure 5a)**. The error bars for the *c* lattice parameter mostly fall within the symbol size in the graph.

The samples become fully tetragonal between 120 and 170 min with $a = b = 3.8883(10)$ Å, **Figure 5a)**. Oxygen still seems to be leaving the samples as the *c*-axis still increases after 120 min, although at a much smaller rate, before a plateau at 11.8445(10) Å is reached. Afterwards, the *c* lattice parameter does not change significantly.

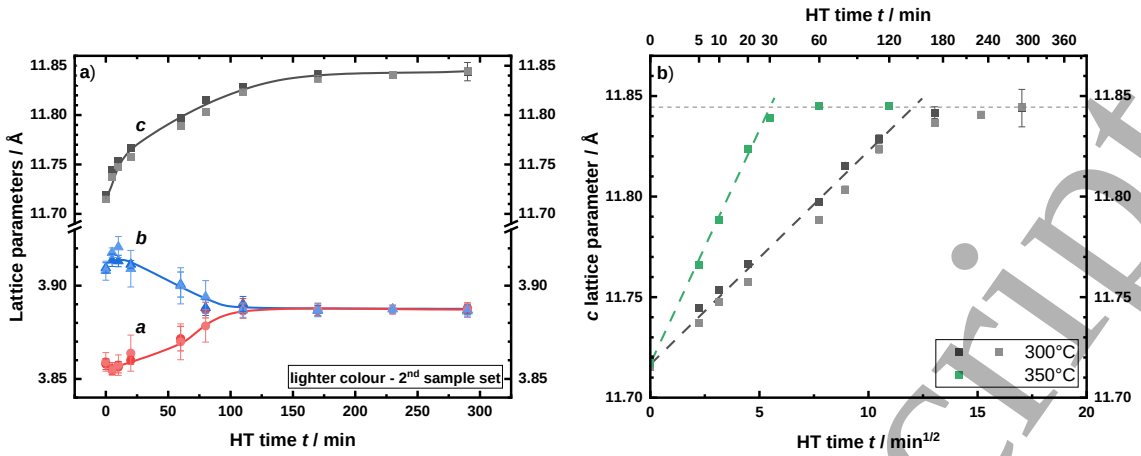

Figure 5: Change of lattice parameters with HT time. **a)** Lattice parameters over HT time *t* of the sample treated at 300 °C. The error bars are one standard deviation. The lines are guides to emphasize the trends. The lattice parameters *b* (blue symbols) and *a* (red symbols) do not change significantly in the first 20 min. After that, the O/T transition begins. This process is finished at around 120 min and *a* and *b* do not change anymore. The *c* lattice parameter (grey symbols) changes according to a square root law up to 120 min as shown in **b)**, indicating a constant rate of *c*-axis change as long as oxygen diffuses out of the crystal structure. An increase in *T* results in an increase in the rate of *c*-axis change.

Looking at the rate of change of the *c*-axis, **Figure 5b)**, two things stand out: Firstly, the rate of change seems to follow a $\sqrt{t}$-dependence up to the point at which a plateau is reached. This is illustrated by the fact that the *c*-axes of all sample sets plotted against $\sqrt{t}$ show a clear linear trend. Secondly, an increase of the HT temperature to 350 °C (green curve) leads to an increase of the rate of change of the *c*-axis – a typical behavior of diffusion-controlled processes [22]. We believe it is safe to assume that the rate of change of the *c*-axis is proportional to the amount of oxygen out-diffusion and linked to the oxygen diffusion coefficients in REBCO [23–26] but different types of experiments need to be done to understand the nature of the observed $\sqrt{t}$ dependency. More important for the purpose of this paper is the fact that the endpoint of the diffusion experiment and the state of maximal oxygen deficiency is reached for the given HT temperatures, because the rate of c-axis change and thus the amount of out-diffusing oxygen approaches zero in the end.

To check these results for their reproducibility, a 2nd sample set was heat-treated at 300 °C, which can be seen in lighter colour in **Figure 5** and **Figure 6**. Due to the fact that this sample set almost mirrored the original set, we regard our procedure as reproducible and we decided to forgo the recreation of the 350 °C sample set.

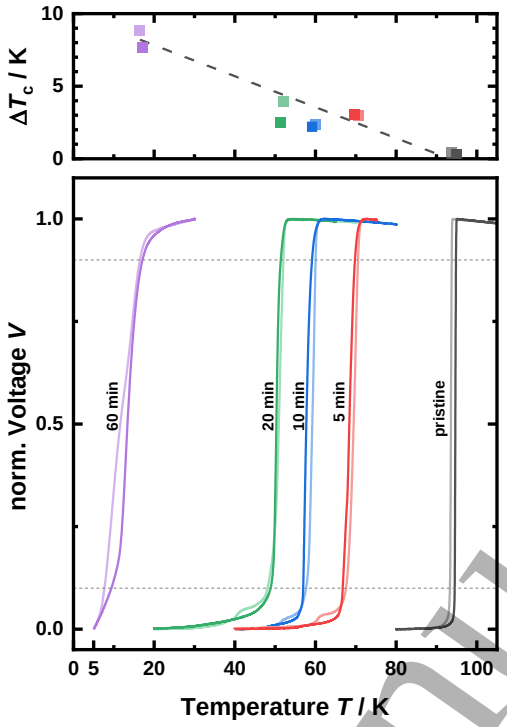

Figure 6: Superconducting transition measured inductively depending on HT time for the 300 °C sample sets (lighter color for 2nd set). T_c^{90} and T_c^{10} are indicated by dotted lines. The sharpness of the transition ΔT_c is shown in the upper panel. With increasing HT time, a clear broadening of the transition can be seen. In addition, a "foot structure" develops at low voltages.

As seen in **Figure 6**, the shape of the superconducting transition changes with increasing HT time, here for 300 °C annealing temperature. The sharpness is captured by ΔT_c in the upper panel of **Figure 6**. The transition is sharpest in the pristine state and increases with increasing HT time, as more and more oxygen diffuses out of the crystal structure. After that, the onset of T_c is below 5 K, the limit of our testing stand.
While the behavior near T_c^{onset} does not change drastically up to the 60 min mark, the transition into the superconducting state (norm. V = 0) starts to develop a so-called "foot structure", which might stem from local parts of the samples having a different oxygen order and thus lower T_c.

Thin films possess too little sample volume for the classical routes of determining the oxygen content via titration [27, 28] or thermogravimetry [10, 29]. Thus, ToF-SIMS was used in an attempt to investigate the chemical composition of a subset of our thin film samples.
ToF-SIMS depth profiling, **Figure 7a)**, reveals that the pristine films have a homogenous chemical composition throughout the film thickness. For heat-treated samples, we find the same result (data not shown) as concluded from constant Sm, Ba, Cu, and O signals over the sputter beam fluence. This agrees with our XRD results, in which we only detect a single phase of SmBCO, **Figure 4**. No apparent diffusion layers developed during the HT.

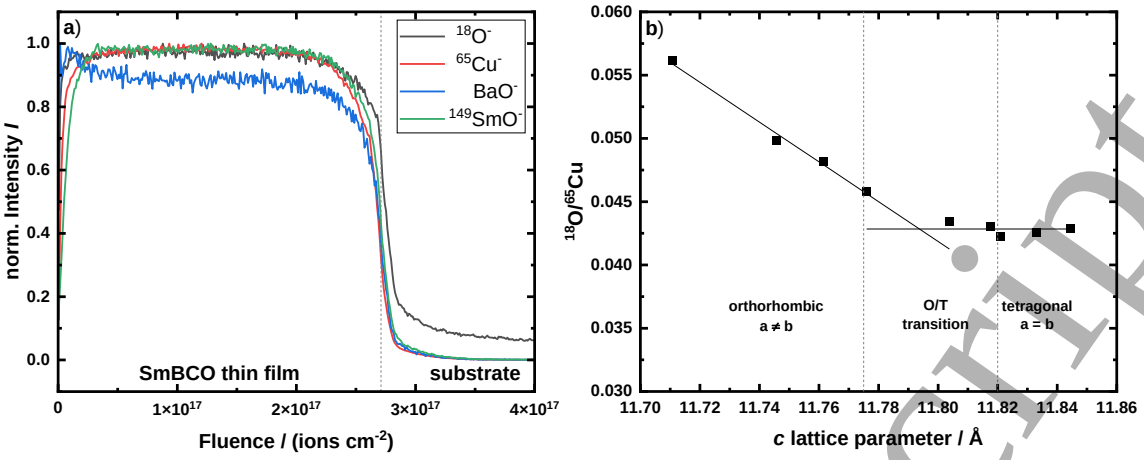

Figure 7: ToF-SIMS investigations: **a)** Depth profile of selected ion species of a pristine sample. The composition is homogenous over the whole film thickness. The substrate interface can be clearly identified. **b)** ^{18}O/^{65}Cu ratio over the *c* lattice parameter of investigated thin film samples. The linear behavior changes drastically at the O/T transition.

The goal of employing ToF-SIMS was to quantify the oxygen content of the samples based on the recorded depth-integrated ^{18}O signals in order to establish a relationship between lattice parameters and chemical composition. However, this is only possible if the ion yield stays constant over the investigated range of δ. Therefore, the signal intensities are summed up to the superconductor/substrate interface and compared to the prominent ^{65}Cu signal as an internal standard, to compensate for slight changes in film thickness and erosion beam currents between the samples.

Unfortunately, the results demonstrate that the ion yields are not constant for the samples, since there is a clear change in slope of the ^{18}O/^{65}Cu ratio as a function of the *c* lattice parameter in the range of 11.775 - 11.82 Å, **Figure 7b)**. The dotted lines were drawn on the basis of the *a* and *b* lattice parameters and whether the thin film samples are orthorhombic, transitional or tetragonal. Considering this, it becomes clear that the ion yields are changing while the crystal structure is transitioning from the orthorhombic to the tetragonal unit cell.

It is not obvious why the thin film samples behave like that. The ion yield is predominantly governed by two factors: sputter rate and ionization rate. Both components combined are called the SIMS matrix effect, meaning that the overall composition of a sample can affect the ionization yields of individual secondary ions [30–32]. A subtle change in crystal structure, as in this case, is unlikely to affect the sputter rate. This is backed by the fact that the superconductor/substrate interface is always detected at the same fluence. This leads to the conclusion that the sputter rate does not change significantly with δ.

The second component to be considered, the ionization rate, is influenced by the valence of the ion species. The valence state affects the ionization probability (electron affinity in case of negatively charged secondary ions) and hence the signal strength of the secondary ions of the metal oxo clusters. This means that changes in the composition-dependent valence states would result in altered ionization rates and thus varying ion yields with δ, which might explain the changing ion yields shown in **Figure 8** (normalized to δ = 0).

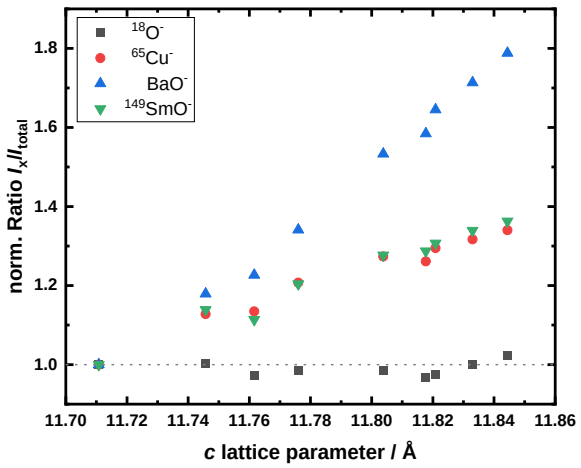

Figure 8: Ion yield as ratio of overall intensity normalized to sample with smallest δ/smallest *c* lattice parameter. The ^{18}O signal is actually the most stable across all samples, indicating that ToF-SIMS is not suited for quantifying the oxygen content in REBCO thin films in absolute values.

The ^{18}O ion yield is the most stable one, while the ^{65}Cu, BaO and ^{149}SmO ion yields increase over the investigated range. This means that the $^{18}O/^{65}Cu$ ratio shown in **Figure 7b)** does not change because of less ^{18}O but more ^{65}Cu being detected. This seemingly odd behavior is backed by Ref. [10], in which Cava et al. have shown that the valence states, or more precisely the bond valence sum, of Y, Ba, and Cu change with δ due to changes in the metal-oxygen bond lengths, and that a significant change in the valence state of Cu can be detected at the O/T transition.

This very dynamic ion yield landscape made it impossible to utilize ToF-SIMS to quantify the oxygen content in absolute numbers. This apparent failure can nevertheless still be used to identify the O/T transition range. From ToF-SIMS, we determined that the crystal structure of the thin film changes when the *c* lattice parameter is in the range of 11.775-11.82 Å, which in turn helps us to determine the critical oxygen deficiency δ_c of thin film samples heat-treated at 300-350 °C more accurately.

5. Discussion

The goal of establishing an alternative way to determine the oxygen deficiency of thin film REBCO samples by using the structural relationship between the lattice parameters and the oxygen deficiency was achieved. This was possible because the *c* lattice parameter increases linearly in the orthorhombic as well as in the tetragonal region.

Because the amount of crystallographic literature data on SmBCO is very limited, powder experiments were conducted first to establish the structural relationship between the lattice parameters and δ. The results are shown in **Figure 9**. The lattice parameters *a* and *b* help to easily identify the orthorhombic and tetragonal regions. The *c* lattice parameter shows a distinct linear behavior in both regions, as described with the following equations:

orthorhombic	$c = (0.102\delta + 11.7275)$ Å	2
Tetragonal	$c = (0.099\delta + 11.7587)$ Å	3

As already alluded to in **Figure 2**, while the behavior of the *c* lattice parameter seems to be fundamentally governed by the linear trends in the orthorhombic and tetragonal phases, the O/T transition behavior is controlled via the HT conditions.

This can be seen if the crystal structure information of our powder samples is combined with the phase boundary information, $T_{O/T}$ and δ_c, of **Figure 1a)** in **Figure 9**. Assuming thermodynamic equilibrium is reached during annealing and a sufficiently rapid quench, heat-treating powder samples at $T < 450$ °C ($pO_2 = 0$ bar) results in δ values much lower than their respective δ_c and thus orthorhombic crystal structures are found. Complementary, δ values of powder samples heat-treated at $T > 500$ °C ($pO_2 = 0$ bar) are bigger than δ_c and thus tetragonal. If, however, the HT conditions are tailored in such a way that the resulting δ is close to δ_c, a transitional sample is produced. Transitional meaning that neither a highly orthorhombic nor tetragonal unit cell can be identified via XRD.

All these cases can be found in the present data. All powder samples heat-treated below $T < 450$ °C exhibit $\delta < \delta_c(400\ °C)$ and are consequently orthorhombic. The tetragonal case, $\delta > \delta_c$, can be found for all samples heat-treated at $T \geq 500$ °C, and the last case, $\delta \approx \delta_c$, is fulfilled for the 450 °C sample, which we consider to be in a transitional state judging from the *a* and *b* lattice parameters. The transitional state is in fact only a mixture of local portions of a powder sample already being tetragonal while other still remaining orthorhombic. Annealing this sample at $T > 450$ °C would trigger the transition of the remaining orthorhombic parts. The reverse would also be possible. If the annealing temperature is kept below 450 °C.

Consider the powder sample heat-treated at 500 °C with $\delta = 0.52$. Its δ is bigger than $\delta_c(500\ °C) \approx 0.4$ but smaller than $\delta_c(275\ °C) \approx 0.6$. We postulate as part of a future study, that the oxygen order of this sample can be reestablished by annealing at $T < 400$ °C and that superconductivity would reemerge as a result of this low-temperature annealing.

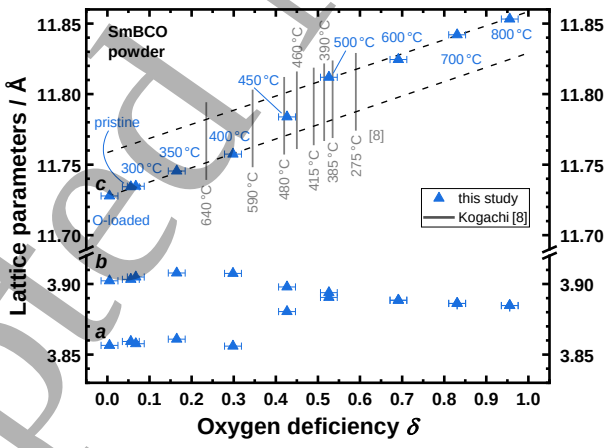

Figure 9: Lattice parameters of SmBCO powder samples as a function of the oxygen deficiency δ. The O/T transition data of Ref. [8] is also plotted (solid grey lines). The *c* lattice parameter shows a linear behavior (dashed black lines) in the orthorhombic and tetragonal phase region with the transition point lying at δ_c. The δ_c position of the O/T transition is temperature-dependent.

Therefore, it can be concluded that the *c* lattice parameter seems to be governed by the linear behavior (equations 2,3) and the critical oxygen deficiency δ_c, which is influenced by the HT conditions. Once the O/T transition is initiated at δ_c, the *c* lattice parameter increases rapidly

to the tetragonal linear trend. This stands in contrast to the often stated continuously changing c lattice parameter behavior [9, 11].

The determined linear dependencies *c* vs. δ of the powder samples can now be used to determine the oxygen deficiencies δ of the thin film samples via the *c* lattice parameter of the films. However, if the *c* lattice parameters of pristine thin film samples are used in equation 2, negative δ values result, which shows that the crystal structure of the powder and thin film samples cannot be compared directly.

The thin films are most likely thermally strained. The thermal strain ε is induced by crystallization at elevated temperatures and the difference of the thermal expansion coefficients (CTE) between film and substrate. In order to evaluate the effect of thermal strain on our analysis, a simple model is assumed. The thermal strain ε is calculated as

$$\varepsilon = \Delta T \cdot (\alpha_{\mathrm{film}} - \alpha_{\mathrm{subst}}), \qquad 4$$

with ΔT being the temperature difference between crystallization and end temperature (room temperature in this case) and the α values are the CTE for film and substrate respectively. To estimate the effect of thermal strain on the crystal structure using equation 4, we set the following boundary conditions:

(1) Relaxation of thermal strain happens towards the free surface. This means for (001) textured films the thermal strain along the *c*-axis $\varepsilon_{\mathrm{thermo,c}}$ becomes zero. This leaves the relevant strain components in the *ab*-plane.
(2) The thermal strain active in the *ab*-plane was evaluated with the averaged CTE along the *a* and *b* direction of SmBCO, resulting in $\varepsilon_{\mathrm{thermo,ab}}$.
(3) Lastly, as $\varepsilon_{\mathrm{thermo,c}} = 0$, the strain remaining along the *c*-axis ε_{c} after cooling is the result of transverse contraction due to the thermal strain in the *ab*-plane.

The remaining strain along the *c*-axis was approximated using the following equation:

$$\varepsilon_{\mathrm{c}} = \varepsilon_{\mathrm{thermo,ab}} \cdot (-\upsilon), \qquad 5$$

with υ being the Poisson's ratio of SmBCO. $\upsilon_{\mathrm{SmBCO}}$ is, to the author's knowledge, only available for SmBCO tape CC [33], where it is given as 0.24-0.26. Even though $\upsilon_{\mathrm{SmBCO}}$ is determined in Ref [33], it is not entirely clear whether the value given for $\upsilon_{\mathrm{SmBCO}}$ was corrected for the influence of the composite structure of a coated conductor tape. Thus, literature data for the Poisson's ratio of single-crystal YBCO was used. Different publications report values of 0.24 [34, 35] – 0.29 [36]. For the strain correction, we settle for a medium value of 0.275, which is in reasonable agreement with $\upsilon_{\mathrm{SmBCO}}$ from Ref. [33].

Table 2 summarizes CTE literature values for different relevant substrate and REBCO materials.

Table 2: Table of CTE for different substrate and thin film materials

Material	Coefficient of thermal expansion (CTE) [10^{-6} K^{-1}]	Temperature range [K]	Reference
LAO	5.7 – 10	270 - 1070	[37, 38]
STO	10.8	270 - 1800	[39]
MgO	10 – 15	270 - 1200	[40, 41]

YBCO	~11-13 (*ab*-plane)	295 - 670	[42–44]
SmBCO	~11.8-13.5 *(ab*-plane)	370 - 870	calculated from [8]

With a temperature difference of 550 K and a difference of the CTEs of LAO and SmBCO of 3.5 10^{-6} K^{-1}, the *ab*-plane is under tensile load with a thermal strain of 0.19 %. This equates to a compressive strain along the *c*-direction of -0.05 %.

The plausibility of these strains must be put in context of certain weak points of this strain correction. Firstly, the CTE of LAO is temperature-dependent, while we assume a constant value of 10 for this simple model. Furthermore, the CTE of SmBCO is likely also temperature-dependent; yet no reliable data was found on this matter. Thus, we believe that this leads to obvious inaccuracies.

Secondly, microstructural features such as lattice misfit, defects or the twin formation were not considered. While the lattice misfit may be alleviated via domain matching epitaxy [45], the influence of defects and/or twin domain formation on the strain state cannot be dismissed [46–48]. This will become clear when the results of the correction are discussed.

Third and finally, we consider the elastic properties of SmBCO to be independent of its chemical composition, δ, and temperature. A study on YBCO [34] has shown that the elastic properties can vary significantly by altering the sample preparation method, implying that the elastic properties and thus also $\upsilon_{\mathrm{SmBCO}}$ is most likely δ-dependent. We consider a constant $\upsilon_{\mathrm{SmBCO}}$ but as mentioned before a range of 0.24 - 0.29 is reported for υ_{YBCO}. Therefore, assuming a constant $\upsilon_{\mathrm{SmBCO}}$ likely introduces further inaccuracy.

Ultimately, this simple strain correction model may not fully describe the strain state of the thin film samples. Yet, these simple considerations yield a strain value in a plausible order of magnitude, which supports the assumption that the model is sufficient for the aim of this paper. Further and deeper investigations into the subject of thermal strain are needed to derive a more comprehensive model for REBCO thin film samples.

With these considerations, the lattice parameters of the thin film samples are corrected as shown in **Figure 10**. The corrected *c* lattice parameters are fitted with the linear trends of the powder data. The lattice parameters *a* and *b* are used to identify whether the sample is orthorhombic, tetragonal, or in the transitional state.

As can be seen in **Figure 10a)**, all data sets are in very good agreement with one another. The thin film samples were heat-treated at 300 or 350 °C and thus exhibited a δ_c of 0.55 - 0.6, which was reinforced by the ToF-SIMS measurements identifying the corresponding *c* lattice parameter range for the O/T transition. The O/T transition is modelled using a logistics function with the center at δ = 0.575. As already mentioned, inaccuracies arise due to the simplicity of the used thermal strain model. δ is determined with an estimated uncertainty of 0.03.

As can be seen, the pristine samples (smallest δ) still show negative δ values, a clear sign that the strain in the system was underestimated. In order to achieve non-negative δ the strain in the *ab*-plane must be thrice as high as currently estimated. This applies to the orthorhombic phase only. If triple the strain correction is applied to the tetragonal phase, δ values beyond 1 would be achieved. Therefore, our simple strain model is a good approximation of the strain in the tetragonal system, and microstructural features such as twin domain boundaries, which are only present in the orthorhombic phase, may play an important role in the strain state of the orthorhombic phase.

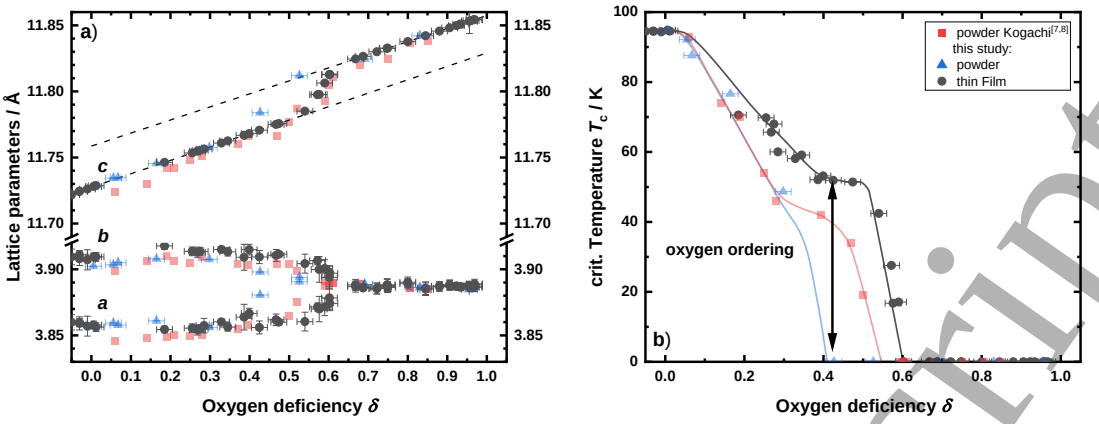

Figure 10: Relationship between oxygen deficiency and (corrected) crystal structure data (a) as well as T_c (b) of SmBCO thin films (black) in comparison to the powder data shown above. Shared legend shown in b). The powder data is more transparent to aid readability. The lattice parameters *a* and *b* are in very good agreement with this determination. The thin films show a higher and sharper T_c plateau than the powder samples due to a higher degree of oxygen ordering along the Cu-O chains [14]. The black arrow in b) highlights the important role of oxygen order at comparable oxygen deficiencies.

The strained crystal structure also seems to influence T_c. This can be seen in **Figure 10b)** showing T_c vs. δ for different powder and thin film data sets. The solid lines are guides to illustrate the general trend of each set. T_c starts out at 94 K for all sets and begins to drop before δ = 0.1. As already explained, the powder sets differ at δ >0.3 due to a slower cooling process in Kogachi et al.'s experiment [7], which leads to reestablishment of oxygen order and thus a narrow T_c plateau at 45 K emerged. This observation matches calculations by Veal et al. [14]. They show how disorder in the Cu-O chains controls the height and shape of the T_c plateau at medium oxygen deficiencies. By cooling the powder samples more rapidly than Kogachi et al., we preserve the disorder in the Cu-O chains of the high-temperature state and thus suppress superconductivity in this δ region. Applying this reasoning to the thin film samples, we conclude that the thin film samples show a very high degree of oxygen ordering. The T_c plateau at 52 K is 7 K higher than that of the powder samples. Furthermore, it is much sharper, which matches with the highly ordered Ortho II phase [14, 20, 21].

Furthermore, it becomes obvious that thin films behave fundamentally different when it comes to the deoxygenation. The maximum δ in thermodynamic equilibrium at 300 °C is given by the isobar *T*-δ line (pO_2 = 0 bar) and is for the presented powder samples below 0.1. Thin films, however, were almost completely deoxygenated under virtually the same HT conditions. This is particularly important for quench events in CC. Even quenches at relatively low temperature that would be unproblematic for bulk SmBCO, pose a real threat to the oxygenation state of SmBCO in thin film form. The origin for the increased diffusivity of oxygen in thin films cannot be determined from the data presented in this study but is plausible that thin films might have unique features such as coherent defects and/or strained crystal structures that play an important role in increasing the oxygen diffusivity along the Cu-O chains and thereby help to establish strong oxygen ordering but also favoring the deoxygenation of the crystal lattice.

6. Conclusion

In this investigation, we have shown how the oxygen deficiency δ of thin film REBCO samples can be determined non-destructively by XRD. We used conventional methods of determining

δ on SmBCO powder samples to establish the crystal structural relationship between the lattice parameters *a*, *b* and *c* and the oxygen deficiency δ.

The obtained powder data set was in very good agreement with published data on SmBCO. The *c* lattice parameter depends linearly on δ in both the orthorhombic and the tetragonal phase. These linear dependencies were then applied to the thin film system. It turned out that the two sample types, powder and thin film, are not directly comparable because thin films are strained epitaxially and thermally.

A simple model was used to estimate the thermal strain. The boundary conditions and weak points of this model were discussed. Nonetheless, the model yielded strain values in a plausible order of magnitude. It was found that a SmBCO thin film on LAO as a substrate is most likely under thermally induced tensile load. The size of the thermal strain is in the range of 0.2 %. The strained *ab*-plane resulted in a compressed *c* lattice parameter due to transverse contraction. This strain correction was applied to the lattice parameters, and a better comparison of the powder and thin film samples was achieved.

The strain model produced very good results in the tetragonal phase, while the strain in the orthorhombic phase was most likely underestimated by a factor of 3, because microstructural features such as domain boundaries were not considered. Only the crystal structure information was used to determine δ. Yet, the superconducting properties, or T_c for that matter, showed a typical behavior for REBCO. Again, the comparison of the powder and thin film samples yielded further insight. We could not only confirm previous investigations, but also show experimental results that demonstrate that the height and shape of the T_c plateau depend more on the oxygen ordering than on the oxygen deficiency itself. The thin film samples therein showed the highest degree of oxygen ordering, as their T_c plateau was 7 K higher and much sharper than that of the powder samples. Possible reasons for this behavior might be a better oxygen diffusivity facilitated by a strained crystal structure or other defects such as domain boundaries or dislocations.

Thus, the presented way of determining δ in thin film samples aids the effort to improve the superconducting properties of REBCO Coated Conductors by means of a non-destructive structural analysis.

7. Data Availability Statement

The data that support the findings of this study are available upon request from the authors.

8. References

[1] Knoth K, Engel S, Apetrii C, Falter M, Schlobach B, Hühne R, Oswald S, Schultz L and Holzapfel B 2006 *Current Opinion in Solid State and Materials Science* **10** 205–16

[2] Obradors X, Puig T, Ricart S, Coll M, Gazquez J, Palau A and Granados X 2012 *Supercond. Sci. Technol.* **25** 123001

[3] Paranthaman M P and Izumi T 2004 *MRS Bull.* **29** 533–41

[4] Erbe M, Cayado P, Freitag W, Ackermann K, Langer M, Meledin A, Hänisch J and Holzapfel B 2020 *Supercond. Sci. Technol.* **33** 94002

[5] Kubo Y, Nakabayashi Y, Tabuchi J, Yoshitake T, Ochi A, Utsumi K, Igarashi H and Yonezawa M 1987 *Jpn. J. Appl. Phys.* **26** L1888

[6] Nakabayashi Y, Kubo Y, Manako T, Tabuchi J, Ochi A, Utsumi K, Igarashi H and Yonezawa M 1988 *Jpn. J. Appl. Phys.* **27** L64

[7] Kogachi M, Nakanishi S, Nakahigashi K, Sasakura H, Minamigawa S, Fukuoka N and Yanase A 1989 *Jpn. J. Appl. Phys.* **28** L609

[8] Kogachi M, Nakahigashi K, Minamigawa S and Nakanishi S 1990 *Jpn. J. Appl. Phys.* **29** L911

[9] Jorgensen, Veal, Paulikas, Nowicki, Crabtree, Claus and Kwok 1990 *Physical review. B, Condensed matter* **41** 1863–77

[10] Cava R J, Hewat A W, Hewat E A, Batlogg B, Marezio M, Rabe K M, Krajewski J J, Peck W F and Rupp L W 1990 *Physica C: Superconductivity* **165** 419–33

[11] Ye and Nakamura 1993 *Physical review. B, Condensed matter* **48** 7554–64

[12] Cava R J, Batlogg B, Rabe K M, Rietman E A, Gallagher P K and Rupp L W 1988 *Physica C: Superconductivity* **156** 523–7

[13] Claus H, Yang S, Paulikas A P, Downey J W and Veal B W 1990 *Physica C: Superconductivity* **171** 205–10

[14] Veal B W and Paulikas A P 1991 *Physica C: Superconductivity* **184** 321–31

[15] Erbe M, Hänisch J, Freudenberg T, Kirchner A, Mönch I, Kaskel S, Schultz L and Holzapfel B 2014 *J. Mater. Chem. A* **2** 4932

[16] Nelson J B and Riley D P 1945 *Proc. Phys. Soc.* **57** 160–77

[17] Pietsch U, Holý V and Baumbach T 2004 *High-Resolution X-Ray Scattering: From Thin Films to Lateral Nanostructures (Springer eBook Collection)* (New York, NY: Springer)

[18] Wimbush S C, Li M, Vickers M E, Maiorov B, Feldmann D M, Jia Q and MacManus-Driscoll J L 2009 *Adv. Funct. Mater.* **19** 835–41

[19] Kogachi M, Nakanishi S, Nakahigashi K, Minamigawa S, Sasakura H, Fukuoka N and Yanase A 1988 *Jpn. J. Appl. Phys.* **27** L1228

[20] Fontaine D de, Wille L T and Moss S C 1987 *Physical review. B, Condensed matter* **36** 5709–12

[21] Fontaine D de, Ozolins V, Islam Z and Moss S C 2005 *Phys. Rev. B* **71**

[22] Paul A, Laurila T, Vuorinen V and Divinski S V 2014 *Thermodynamics, diffusion and the Kirkendall effect in solids* (Cham, Heidelberg: Springer)

[23] Routbort J L and Rothman S J 1994 *Journal of Applied Physics* **76** 5615–28

[24] Tsukui S, Adachi M, Oshima R, Nakajima H, Toujou F, Tsukamoto K and Tabata T 2001 *Physica C: Superconductivity* **351** 357–62

[25] Tsukui S, Koritala R E, Li M, Goretta K C, Adachi M, Baker J E and Routbort J L 2003 *Physica C: Superconductivity* **392-396** 841–6

[26] Lu J, Xin Y, Jarvis B and Bai H 2021 *Supercond. Sci. Technol.* **34** 75004

[27]Nedeltcheva T K, Georgieva S IV, Vladimirova L K and Stoyanova-Ivanova A K 2009 *Talanta* **77** 1745–7
[28]Georgieva S, Nedeltcheva T and Stoyanova-Ivanova A 2016 *ACSJ* **13** 1–15
[29]Ghigna P, Spinolo G, Malavasi L, Chiodelli G and Flor G 2001 *Phys. Chem. Chem. Phys.* **3** 606–12
[30]Deline V R, Katz W, Evans C A and Williams P 1978 *Appl. Phys. Lett.* **33** 832–5
[31]Seah M P and Shard A G 2018 *Applied Surface Science* **439** 605–11
[32]Priebe A, Xie T, Bürki G, Pethö L and Michler J 2020 *J. Anal. At. Spectrom.* **35** 1156–66
[33]Osamura K, Machiya S, Tsuchiya Y, Suzuki H, Shobu T, Sato M and Ochiai S 2012 *IEEE Trans. Appl. Supercond.* **22** 8400809
[34]Lei M and Ledbetter H 1991 *NIST Interagency Reports*
[35]Reichardt W, Pintschovius L, Hennion B and Collin F 1988 *Supercond. Sci. Technol.* **1** 173–6
[36]Jong M de *et al* 2015 *Scientific data* **2** 150009
[37]Vourdas N, Marathoniti E, Pandis P K, Argirusis C, Sourkouni G, Legros C, Mirza S and Stathopoulos V N 2018 *Transactions of Nonferrous Metals Society of China* **28** 1582–92
[38]Inaba H 2001 *Solid State Ionics* **144** 99–108
[39]Ligny D de and Richet P 1996 *Physical review. B, Condensed matter* **53** 3013–22
[40]R R Reeber, K Gossel and Kai Wang 1995 *European Journal of Mineralogy* **7** 1442
[41]Dubrovinsky L S and Saxena S K 1997 *Phys Chem Min* **24** 547–50
[42]Scherer T, Marienhoff P, Herwig R, Neuhaus M and Jutzi W 1992 *Physica C: Superconductivity* **197** 79–83
[43]Zeisberger M, Latka I, Ecke W, Habisreuther T, Litzkendorf D and Gawalek W 2005 *Supercond. Sci. Technol.* **18** S202-S205
[44]Yamada Y, Kawashima J, Wen J-G, Niiori Y and Hirabayashi I 2000 *Jpn. J. Appl. Phys.* **39** 1111
[45]Narayan J and Larson B C 2003 *Journal of Applied Physics* **93** 278–85
[46]Specht E D, Sparks C J, Dhere A G, Brynestad J, Cavin O B, Kroeger D M and Oye H A 1988 *Physical review. B, Condensed matter* **37** 7426–34
[47]Jou C J and Washburn J 1989 *J. Mater. Res.* **4** 795–801
[48]Guzman R, Gazquez J, Rouco V, Palau A, Magen C, Varela M, Arbiol J, Obradors X and Puig T 2013 *Appl. Phys. Lett.* **102** 81906